DEUTSCHES ELEKTRONEN – SYNCHROTRON

DESY 93-068
May 1993

Hadronic Energy Distributions in Deep-Inelastic Electron-Proton Scattering

ZEUS Collaboration

ISSN 0418-9833

NOTKESTRASSE 85 · D-2000 HAMBURG 52

To be sure that your preprints are promptly included in the HIGH ENERGY PHYSICS INDEX, send them to (if possible by air mail):

DESY Bibliothek Notkestraße 85 W-2000 Hamburg 52 Germany	DESY-IfH Bibliothek Platanenallee 6 O-1615 Zeuthen Germany

DESY 93-068
May 1993

ISSN 0418-9833

Hadronic Energy Distributions In Deep-Inelastic Electron-Proton Scattering

ZEUS Collaboration

May 19, 1993

Abstract

This paper presents energy distributions of the hadronic system produced in neutral-current electron-proton deep-inelastic scattering at a centre of mass energy of 296 GeV. Comparison of the results with QCD Monte Carlo models shows that QCD radiation has a strong influence on the characteristics of the final state. The data are reasonably reproduced by the Lund model based on a matrix element calculation in first order of α_s, followed by appropriate parton showers, as well as by the colour dipole model. The HERWIG parton shower model also gives a reasonable representation of the data. Neither the first order matrix elements alone nor the Lund parton shower model, without the matrix element calculation, reproduce the data.

The ZEUS Collaboration

M. Derrick, D. Krakauer, S. Magill, B. Musgrave, J. Repond, S. Repond, R. Stanek, R.L. Talaga, J. Thron
Argonne National Laboratory, Argonne, IL, USA [n]

F. Arzarello, R. Ayad[1], G. Bari, M. Basile, L. Bellagamba, D. Boscherini, A. Bruni, G. Bruni, P. Bruni, G. Cara Romeo, G. Castellini [2], M. Chiarini, L. Cifarelli, F. Cindolo, F. Ciralli, A. Contin, S. D'Auria, C. Del Papa, F. Frasconi, P. Giusti, G. Iacobucci, G. Laurenti, G. Levi, Q. Lin,B. Lisowski, G. Maccarrone, A. Margotti, T. Massam, R. Nania, C. Nemoz, F. Palmonari, G. Sartorelli, R. Timellini, Y. Zamora Garcia[1], A. Zichichi
University and INFN Bologna, Bologna, Italy [f]

A. Bargende, J. Crittenden, H. Dabbous[3], K. Desch, B. Diekmann, T. Doeker, M. Geerts, G. Geitz, H. Hartmann, D. Haun, K. Heinloth, E. Hilger, H.-P. Jakob, S. Kramarczyk, M. Kückes[4], A. Mass, S. Mengel, J. Mollen, D. Monaldi[5], H. Müsch[6], E. Paul, R. Schattevoy, J.-L. Schneider, D. Schramm, R. Wedemeyer
Physikalisches Institut der Universität Bonn, Bonn, Federal Republic of Germany [c]

A. Cassidy, D.G. Cussans, N. Dyce, B. Foster, R. Gilmore, G.P. Heath, H.F. Heath, M. Lancaster, T.J. Llewellyn, J. Malos, C.J.S. Morgado, R.J. Tapper, S.S. Wilson, R. Yoshida
H.H. Wills Physics Laboratory, University of Bristol, Bristol, U.K. [m]

R.R. Rau
Brookhaven National Laboratory, Upton, L.I., USA [n]

M. Arneodo, T. Barillari, M. Schioppa, G. Susinno
Calabria University, Physics Dept.and INFN, Cosenza, Italy [f]

A. Bernstein, A. Caldwell, I. Gialas, J.A. Parsons, S. Ritz, F. Sciulli[7], P.B. Straub, L. Wai, S. Yang
Columbia University, Nevis Labs., Irvington on Hudson,N.Y.,USA [o]

J. Chwastowski[8], A. Dwurazny, A. Eskreys, Z. Jakubowski[9], B. Nizioł, K. Piotrzkowski, M. Zachara, L. Zawiejski
Inst. of Nuclear Physics, Cracow, Poland [j]

B. Bednarek, P. Borzemski, K. Eskreys, K. Jeleń, D. Kisielewska, T. Kowalski, E. Rulikowska-Zarębska, L. Suszycki, J. Zając
Faculty of Physics and Nuclear Techniques, Academy of Mining and Metallurgy, Cracow, Poland [j]

T. Kędzierski, A. Kotański, M. Przybycień
Jagellonian Univ., Dept. of Physics, Cracow, Poland [j]

L.A.T. Bauerdick, U. Behrens, J.K. Bienlein, S. Böttcher, C. Coldewey, A. Dannemann, G. Drews, P. Erhard[10], M. Flasiński[11], I. Fleck, R. Gläser[12], P. Göttlicher, B. Gutjahr, T. Haas, L. Hagge, W. Hain, D. Hasell, H. Hultschig, G. Jahnen[13], P. Joos, M. Kasemann, R. Klanner, W. Koch, L. Köpke, U. Kötz, H. Kowalski, J. Krüger, J. Labs, A. Ladage, B. Löhr, M. Löwe, D. Lüke, J. Mainusch, O. Manczak[14], M. Momayezi, J.S.T. Ng, S. Nickel, D. Notz, K.-U. Pösnecker[15], M. Rohde, J. Roldán[16], E. Ros[8], U. Schneekloth, J. Schroeder, W. Schulz, F. Selonke, E. Stiliaris[16], E. Tscheslog[17], T. Tsurugai, W. Vogel[18], G. Wolf, C. Youngman
Deutsches Elektronen-Synchrotron DESY, Hamburg, Federal Republic of Germany

H.J. Grabosch, A. Leich, A. Meyer, C. Rethfeldt, S. Schlenstedt
DESY-Zeuthen, Inst. für Hochenergiephysik, Zeuthen, Federal Republic of Germany

G. Barbagli, A. Francescato, M. Nuti, P. Pelfer
University and INFN, Florence, Italy [f]

G. Anzivino, R. Casaccia, S. De Pasquale, S. Qian, L. Votano
INFN, Laboratori Nazionali di Frascati, Frascati, Italy [f]

A. Bamberger, A. Freidhof, W. Kröger, T. Poser, S. Söldner-Rembold, G. Theisen, T. Trefzger
Physikalisches Institut der Universität Freiburg, Freiburg, Federal Republic of Germany [c]

N.H. Brook, P.J. Bussey, A.T. Doyle, J.R. Forbes, V.A. Jamieson, C. Raine, D.H. Saxon
Dept. of Physics and Astronomy, University of Glasgow, Glasgow, U.K. [m]

H. Brückmann[19], G. Gloth, U. Holm, H. Kammerlocher, B. Krebs, T. Neumann, K. Wick
Hamburg University, I. Institute of Exp. Physics, Hamburg, Federal Republic of Germany [c]

A. Fürtjes, E. Lohrmann, J. Milewski[14], M. Nakahata[20], N. Pavel, G. Poelz, W. Schott, J. Terron[16], F. Zetsche
Hamburg University, II. Institute of Exp. Physics, Hamburg, Federal Republic of Germany [c]

T.C. Bacon, R. Beuselinck, I. Butterworth, E. Gallo, V.L. Harris, D.B. Miller, A. Prinias, J.K. Sedgbeer, A. Vorvolakos, A. Whitfield
Imperial College London, High Energy Nuclear Physics Group, London, U.K. [m]

T. Bienz, H. Kreutzmann, U. Mallik, E. McCliment, M. Roco, M.Z. Wang
University of Iowa, Physics and Astronomy Dept., Iowa City, USA [n]

P. Cloth, D. Filges
Forschungszentrum Jülich, Institut für Kernphysik, Jülich, Federal Republic of Germany

S.H. An, S.M. Hong, C.O. Kim, T.Y. Kim, S.W. Nam, S.K. Park, M.H. Suh, S.H. Yon
Korea University, Seoul, Korea [h]

L. Chen, R. Imlay, S. Kartik, H.-J. Kim, R.R. McNeil, W. Metcalf
Louisiana State University, Dept. of Physics and Astronomy, Baton Rouge, LA, USA [n]

F. Barreiro[21], G. Cases, L. Hervás[22], L. Labarga[22], J. del Peso, J.F. de Trocóniz[23]
Univer. Autónoma Madrid, Depto de Física Teórica, Madrid, Spain [l]

F. Ikraiam, J.K. Mayer, G.R. Smith
University of Manitoba, Dept. of Physics, Winnipeg, Manitoba, Canada [a]

F. Corriveau, D.J. Gilkinson, D.S. Hanna[7], J. Hartmann, L.W. Hung, J.N. Lim, R. Meijer Drees, J.W. Mitchell, P.M. Patel, L.E. Sinclair, D.G. Stairs, M. St.Laurent, R. Ullmann
McGill University, Dept. of Physics, Montreal, Quebec, Canada [a] [b]

G.L. Bashindzhagyan, P.F. Ermolov, L.K. Gladilin, Y.A. Golubkov, V.A. Kuzmin, E.N. Kuznetsov, A.A. Savin, A.G. Voronin, N.P. Zotov
Moscow State University, Institute of Nuclear Pysics, Moscow, Russia [k]

S. Bentvelsen, M. Botje, A. Dake, J. Engelen, P. de Jong, M. de Kamps, P. Kooijman, A. Kruse, H. van der Lugt, V. O'Dell, A. Tenner, H. Tiecke, H. Uijterwaal[24], M. Vreeswijk, L. Wiggers, E. de Wolf, R. van Woudenberg
NIKHEF-Amsterdam, Netherlands [i]

B. Bylsma, L.S. Durkin, K. Honscheid, C. Li, T.Y. Ling, K.W. McLean, W.N. Murray, I.H. Park, T.A. Romanowski[25], R. Seidlein
Ohio State University, Physics Department, Columbus, Ohio, USA [n]

G.A. Blair, A. Byrne, R.J. Cashmore, A.M. Cooper-Sarkar, R.C.E. Devenish, D.M. Gingrich[26], P.M. Hallam-Baker[8], N. Harnew, T. Khatri, K.R. Long, P. Luffman, I. McArthur, P. Morawitz, J. Nash, S.J.P. Smith[27], N.C. Roocroft, F.F. Wilson
Department of Physics, University of Oxford, Oxford, U.K. [m]

G. Abbiendi, R. Brugnera, R. Carlin, F. Dal Corso, M. De Giorgi, U. Dosselli, F. Gasparini, S. Limentani, M. Morandin, M. Posocco, L. Stanco, R. Stroili, C. Voci
Dipartimento di Fisica dell' Universita and INFN, Padova, Italy [j]

J.M. Butterworth, J. Bulmahn, G. Feild, B.Y. Oh[28], J. Whitmore[29]
Pennsylvania State University, Dept. of Physics, University Park, PA, USA [o]

U. Contino, G. D'Agostini, M. Guida[30], M. Iori, S.M. Mari, G. Marini, M. Mattioli, A. Nigro
Dipartimento di Fisica, Univ. 'La Sapienza' and INFN, Rome, Italy [j]

J.C. Hart, N.A. McCubbin, K. Prytz, T.P. Shah, T.L. Short
Rutherford Appleton Laboratory, Chilton, Didcot, Oxon, U.K. [m]

E. Barberis, N. Cartiglia, C. Heusch, B. Hubbard, J. Leslie, W. Lockman, K. O'Shaughnessy, H.F. Sadrozinski, A. Seiden, D. Zer-Zion
University of California, Santa Cruz, CA, USA [n]

E. Badura, J. Biltzinger, R.J. Seifert, A.H. Walenta, G. Zech
Fachbereich Physik der Universität-Gesamthochschule Siegen, Federal Republic of Germany [c]

S. Dagan[31], A. Levy,
School of Physics, Tel-Aviv University, Tel Aviv, Israel [e]

T. Hasegawa, M. Hazumi, T. Ishii, S. Kasai[32], M. Kuze, Y. Nagasawa, M. Nakao, H. Okuno, K. Tokushuku, T. Watanabe, S. Yamada
Institute for Nuclear Study, University of Tokyo, Tokyo, Japan [g]

M. Chiba, R. Hamatsu, T. Hirose, S. Kitamura, S. Nagayama, Y. Nakamitsu
Tokyo Metropolitan University, Dept. of Physics, Tokyo, Japan [g]

R. Cirio, M. Costa, M.I. Ferrero, L. Lamberti, S. Maselli, C. Peroni, A. Solano, A. Staiano
Universita di Torino, Dipartimento di Fisica Sperimentale and INFN, Torino, Italy [j]

M. Dardo
Facultá di Scienze, University of Torino, Alessandria, and INFN-Sezione di Torino, Torino, Italy [j]

D.C. Bailey, D. Bandyopadhyay, F. Benard, S. Bhadra, M. Brkic, B.D. Burow, F.S. Chlebana, M.B. Crombie, G.F. Hartner, G.M. Levman, J.F. Martin, R.S. Orr, J.D. Prentice, C.R. Sampson, G.G. Stairs, R.J. Teuscher, T.-S. Yoon
University of Toronto, Dept. of Physics, Toronto, Ont., Canada [a]

F.W. Bullock, C.D. Catterall, J.C. Giddings, T.W. Jones, A.M. Khan, J.B. Lane, P.L. Makkar, D. Shaw, J. Shulman
University College London, Physics and Astronomy Dept., London, U.K. [m]

K. Blankenship, J. Kochocki, B. Lu, L.W. Mo
Virginia Polytechnic Inst. and State University, Physics Dept., Blacksburg, VA, USA [o]

K. Charchuła, J. Ciborowski, J. Gajewski, G. Grzelak, M. Kasprzak, M. Krzyżanowski, K. Muchorowski, R.J. Nowak, J.M. Pawlak, A. Stopczyński, T. Tymieniecka, R. Walczak, A.K. Wróblewski, J.A. Zakrzewski, A.F. Żarnecki
Warsaw University, Institute of Experimental Physics, Warsaw, Poland [j]

M. Adamus
Institute for Nuclear Studies, Warsaw, Poland [j]

H. Abramowicz[14], Y. Eisenberg, C. Glasman[33], U. Karshon[31], A. Montag[31], D. Revel, A. Shapira
Weizmann Institute, Nuclear Physics Dept., Rehovot, Israel [d]

C. Foudas, C. Fordham, R.J. Loveless, A. Goussiou, I. Ali, B. Behrens, S. Dasu, D.D. Reeder, W.H. Smith, S. Silverstein
University of Wisconsin, Dept. of Physics, Madison, WI, USA [n]

W.R. Frisken, K.M. Furutani, Y. Iga
York University, Dept. of Physics, North York, Ont., Canada [a]

[1] supported by Worldlab, Lausanne, Switzerland
[2] also at IROE Florence, Italy
[3] now at SAP, Heidelberg
[4] now at TRIUMF, Vancouver
[5] now at Univ. of Bologna
[6] now a self-employed consultant
[7] now at DESY as Alexander von Humboldt Fellow
[8] now at CERN
[9] now at DESY
[10] now at IST GmbH, Darmstadt
[11] on leave from Jagellonian University, Cracow
[12] now at Martin & Associates, Hamburg
[13] now at Harry Hoffmann, Fitzbek
[14] on leave from Warsaw University, Warsaw
[15] now at Lufthansa, Frankfurt
[16] supported by the European Community
[17] now at Integrata, Frankfurt
[18] now at Blohm & Voss, Hamburg
[19] deceased
[20] now at Institute for Cosmic Ray Research, University of Tokyo
[21] on leave of absence at DESY, supported by DGICYT
[22] partially supported by Comunidad Autónoma de Madrid, Spain
[23] supported by Fundación Banco Exterior
[24] now at SSC, Dallas
[25] now at Department of Energy, Washington
[26] now at Centre for Subatomic Research, Univ.of Alberta, Canada and TRIUMF, Vancouver, Canada
[27] now with McKinsey Consultants, Sidney, Australia
[28] on leave and supported by DESY 1992-93
[29] on leave and supported by DESY 1991-92
[30] permanent address Dip. di Fisica, Univ. di Salerno, Italy
[31] supported by the MINERVA Gesellschaft für Forschung GmbH
[32] now at Hiroshima National College of Maritime Technology
[33] supported by the DAAD - Deutscher akademischer Austauschdienst

[a] supported by the Natural Sciences and Engineering Research Council of Canada
[b] supported by the FCAR of Quebec, Canada
[c] supported by the German Federal Ministry for Research and Technology (BMFT)
[d] supported by the MINERVA Gesellschaft für Forschung GmbH, by the Israel Ministry of Energy, and by the Israel Academy of Science
[e] supported by the Israel Ministry of Energy, and by the German Israeli Foundation
[f] supported by the Italian National Institute for Nuclear Physics (INFN)
[g] supported by the Japanese Ministry of Education, Science and Culture (the Monbusho) and its grants for Scientific Research
[h] supported by the Korean Ministry of Education and Korea Science and Engineering Foundation
[i] supported by the Netherlands Foundation for Research on Matter (FOM)
[j] supported by the Polish Government and Ministry of Education Research Programs
[k] supported by the German Federal Ministry for Research and Technology (BMFT), the Volkswagen Foundation, and the Deutsche Forschungsgemeinschaft
[l] supported by the Spanish Ministry of Education and Science through funds provided by CICYT
[m] supported by the UK Science and Engineering Research Council
[n] supported by the US Department of Energy
[o] supported by the US National Science Foundation

1 Introduction

Operation of the HERA electron-proton collider has extended the kinematic range for studies of neutral-current, deep-inelastic scattering (DIS). The beam energies of 26.7 GeV for the electrons and 820 GeV for the protons result in a centre of mass energy of $\sqrt{s} = 296$ GeV, an order of magnitude higher than has been available from fixed-target DIS experiments. In this paper, energy distributions of the final state hadronic system, measured in the HERA laboratory frame, are compared with the predictions of several Monte Carlo models. The data were obtained with the ZEUS detector at the HERA collider and correspond to an integrated luminosity of 30 nb^{-1}. Similar comparisons, using a data set of about 1.6 nb^{-1}, have been published recently by the H1 collaboration [1].

Monte Carlo models that simulate the basic parton level processes, including both the perturbative and non-perturbative phases, have become essential tools in interpreting multi-body final states resulting from high energy interactions. These models allow a simulation of the experimental conditions, but are also needed to interpret the observed data in terms of the underlying parton level processes.

In the case of e^+e^- annihilation, such models give a description of the final hadronic state that can reproduce even fine details of the data [2]. The DIS process is more complex for several reasons: the incoming proton can give rise to initial state QCD radiation, the kinematics of the primary interaction of the exchanged boson depend on more than one variable and, finally, the character of the proton remnant is not well understood. Even so, several models give a satisfactory representation of the lower energy DIS data. The new range of kinematics opened up by the HERA collider allows a more detailed study, particularly of the dependence on the kinematic variables.

Results from the lower energy DIS experiments have shown that perturbative QCD corrections to the naïve quark parton model (QPM) are required to describe the hadronic final state [3, 4]. Our recent observation of two jet production in DIS [5] shows clearly that higher order processes, giving rise to multi-partonic final states, are important at HERA energies and so must be included in the simulations.

2 The ZEUS Detector

ZEUS is a general purpose magnetic detector. A description of the detector, the trigger system and the event selection has been given previously [5, 6]. Here we describe only the detector parts relevant to this analysis.

Charged particle tracks are measured by a cylindrical central-drift-chamber (CTD) [7]. During the data taking period used for this analysis, the single wire resolutions were measured to be $\sigma_z = 4.0$ cm and $\sigma_{r\phi} = 1$ mm. (The ZEUS coordinate system is right-handed with the Z-axis pointing in the direction of the proton beam). The CTD is surrounded by a superconducting solenoid with a thickness of 0.9 radiation lengths, which provided an axial magnetic field of 1.43 T.

A high resolution, uranium scintillator calorimeter (CAL) [8] surrounds the tracking system, covering 99.7% of the solid angle. It is made of three parts, the forward (FCAL), barrel (BCAL)

and rear (RCAL) calorimeters. Each part is segmented longitudinally into an electromagnetic (EMC) and either one or two hadronic (HAC) sections. In test beams, the energy resolution for electrons was measured to be $\sigma(E)/E = 0.18/\sqrt{E}$ and for hadrons $\sigma(E)/E = 0.35/\sqrt{E}$, where E is in GeV [8, 9]. The scintillator tiles form 5918 cells, each of which is read out on two sides. The transverse sizes of the readout cells are typically 5 cm $\times$ 20 cm in the EMC sections of FCAL and BCAL and 10 cm $\times$ 20 cm in the RCAL. The HAC section cells cover four (two) EMC cells in FCAL, BCAL (RCAL) and so are typically 20 cm $\times$ 20 cm in cross section. The nominal interaction point at Z= 0 is approximately 220 cm from the front face of FCAL and 150 cm from that of RCAL.

The absolute energy calibration and the cell to cell uniformity were established in test beam measurements. These calibrations were transferred to the HERA environment using the measured signals induced by the natural radioactivity of the uranium. Both the cell to cell uniformity and the stability of the system are at the 1% level. Although studies indicate that the energy loss in inert material is well described by the detector simulation, except for the region close to the beam pipe [6], the data shown in this paper are not corrected for acceptance, energy losses, and other instrumental effects.

3 Kinematics

Neutral-current, deep-inelastic scattering takes place by the exchange of a virtual boson giving rise to the reaction

$$ep \rightarrow e + \ hadrons. \tag{1}$$

For the present data sample, the reaction is dominated by the exchange of a virtual photon, γ^*. The event kinematics are characterized by Q^2, the negative square of the four-momentum transfer, and the Bjorken scaling variable, x. These quantities are conventionally calculated from the energies of the incoming electron (E_e) and proton (E_p), the energy of the scattered electron (E'_e) and the electron scattering angle (ϑ_e). In lowest order (QPM), the DIS process is just the interaction of this electroweak current with one of the quarks from the incoming proton, $\gamma^* + q \rightarrow q$. The rest of the proton forms the target remnant. Although the basic properties of the final state hadronic system are given by this interaction, the detailed properties reflect higher order QCD effects.

The hadronic final state itself can also be used to determine the event kinematics, in particular through a characteristic angle, γ_h. In the QPM, with massless partons, γ_h would be the laboratory angle of the final state quark. The value of this angle is determined by four-momentum conservation and can be calculated from the transverse and longitudinal energy flow of the hadronic system as [6]:

$$\cos\gamma_h = \frac{(\sum p_X)^2 + (\sum p_Y)^2 - (\sum(E - p_z))^2}{(\sum p_X)^2 + (\sum p_Y)^2 + (\sum(E - p_z))^2} \tag{2}$$

where p_X and p_Y are the transverse momentum components of the particles making up the hadronic system, p_z is the longitudinal component, and E is the energy. In calculating γ_h, the sum over particles is replaced by the sum over calorimeter energy deposits: E is now the

energy measured in the calorimeter cell and p_X, p_Y, and p_z are the cell energies multiplied by appropriate angular factors. Some particles are lost in the forward beam pipe, but they give a small contribution to the above sum.

For reasons previously discussed [6], we measure the variables x and Q^2 from the two angles ϑ_e and γ_h alone (the double angle method):

$$Q^2 = 4E_e^2 \frac{\sin\gamma_h(1+\cos\vartheta_e)}{\sin\gamma_h + \sin\vartheta_e - \sin(\vartheta_e + \gamma_h)} \tag{3}$$

$$x = \left(\frac{E_e}{E_p}\right)\left(\frac{\sin\gamma_h + \sin\vartheta_e + \sin(\vartheta_e + \gamma_h)}{\sin\gamma_h + \sin\vartheta_e - \sin(\vartheta_e + \gamma_h)}\right). \tag{4}$$

The invariant mass, W, of the hadronic system is related to x, Q^2, and the proton mass, m_p, by:

$$W^2 = Q^2\frac{1-x}{x} + m_p^2, \tag{5}$$

and has a maximum value of $\sqrt{s}$.

4 Event Selection and Reconstruction

The events were selected with a three level trigger, as previously described [5, 6], and subsequently processed with the ZEUS off-line reconstruction programs. Minimum energy cuts were applied to the cell energies to reduce the influence of the uranium noise on the reconstruction of the kinematical variables. Scattered electrons were identified by an algorithm based on the properties of electromagnetic showers in the calorimeter [6]. The impact point of the electron on the face of the calorimeter was determined from the distribution of energy among the cells contributing to the electron cluster, as well as from the signal balance between readouts on the two sides of each cell. Charged tracks were reconstructed from hits in the CTD. At least two well measured tracks were required to define a valid event vertex in Z; otherwise it was set to zero.

After reconstruction, the data were passed through filter programs [6] designed to remove events coming from cosmic rays and background events induced by the proton beam alone. After these initial cuts, the following requirements were made:

- $\delta = \sum E(1-\cos\vartheta) > 35$ GeV, where the sum runs over all calorimeter cells. The measured energy of the cell is denoted by E and its polar angle with respect to the incident proton beam by ϑ. This cut removed most of the background from photoproduction events and proton beam-gas events that originated inside the detector system. It also removed DIS events coming from electrons that have emitted an energetic initial state photon.
- Energy in the FCAL greater than 1 GeV. This removed most interactions of the electron beam with the residual gas in the beam pipe as well as possible diffractive events.
- Identification of an isolated electron with an energy greater than 5 GeV. This selection tagged the event as a neutral current candidate.

- $Q^2 > 10$ GeV^2. This implies a fiducial cut on the impact point of the electron close to the RCAL beam pipe.

- $\delta_{had} > 0.04E_e$, where δ_{had} is the hadronic contribution to δ. This ensures that the event kinematics are sufficiently well measured.

A data sample of 2444 events satisfied these selections, of which approximately 70% had a reconstructed vertex. One third of the events were visually inspected to check the purity of the sample. The contamination from cosmic ray interactions and other obvious background sources was at the one percent level. The effect of the residual background from photoproduction reactions is small, as we discuss later, and does not effect the conclusions of the paper.

The distribution of events in the $W^2 - x$ plane is shown in figure 1a. The data reach x values that are two orders of magnitude smaller than have been accessible to previous fixed target experiments in this range of momentum transfer so that the W^2 values extend to almost 10^5 GeV^2. This is much higher than the range of Q^2 seen in figure 1b. This distribution has been normalized to the number of events, N. The distribution also falls rapidly with Q^2, reflecting the dominant effect of the photon propagator, whereas the distribution in W is relatively uniform. The histogram shows, as an example, the prediction of one of the models discussed below. The QPM kinematics are also illustrated in figure 1a by the γ_h contours (full lines) that mark the boundaries between the three parts of the calorimeter. The dashed line shows a 10° contour discussed later.

5 QCD Models and Event Simulation

In describing the structure of the hadronic final state in DIS, it is necessary to include higher order QCD contributions. The exact matrix elements, calculated order by order in the strong coupling constant α_s, can be used to estimate these corrections. However, only partial second order results exist for DIS [10]. Alternatively, models based on the leading logarithm approximation (LLA), with modifications for coherence effects, can be employed. There are several such models: parton showers [11, 12] and colour dipoles [13]. Both the parton shower and colour dipole models describe present e^+e^- data [2] for the radiation of the final state quarks and are in general accord with the lower energy DIS data [14]. The present data, which extends to much lower x values where increased radiation may be expected and where the W^2 and Q^2 values are very different, is a powerful testing ground of the different models.

In addition to the leading order reaction, $\gamma^* + q \to q$, two processes contribute to DIS to first order in α_s: boson-gluon fusion (BGF), $\gamma^* + g \to q + \bar{q}$ and QCD Compton scattering (QCDC), $\gamma^* + q \to q + g$. The exact matrix elements, calculated to first order, are used to simulate these processes. In order to calculate cross-sections for these reactions, a cut on the minimum invariant mass of all pairs of final state partons, $m_{ij}^2 = y_{cut}W^2$, is needed to ensure that they are well behaved. The matrix element calculations are combined with the electroweak scattering cross section in the Monte Carlo program LEPTO [15]. We denote this simulation by ME.

In higher orders, one generally expects several partons in the partonic final state. One model that simulates such multi-parton states is the parton shower (PS) model. In this picture, the struck quark can emit partons either before or after the boson vertex. As the quark is radiating

the initial state shower, before the photon vertex, it becomes more off-shell or virtual. After the interaction, the quark may again be off mass-shell and returns to the mass-shell by radiating the final state shower. The magnitude and hardness of the radiation are limited by the maximum virtuality (invariant mass) of the struck quark just before and just after the interaction with the virtual photon. In DIS this maximum virtuality scale is not well defined and could, in principle, be any function of Q^2 and/or W^2 [11].

In this paper, we show the predictions of two extreme choices of virtuality scale that are available in LEPTO, Q^2 and W^2, denoted by PS(Q^2) and PS(W^2), respectively. Although neither choice is theoretically satisfactory, they span the range of possibilities predicted by this model. An intermediate scale, based on the limiting behaviour of the matrix elements at low and high x is given by $Q^2(1-x)max(1, \ln\frac{1}{x})$ [15]. We denote the parton shower model with this scale by PS($Q^2(1-x)$). Interference between the initial and final state showers is neglected in LEPTO. Since typical Q^2 values are quite low, the predictions of the PS(Q^2) model will be close to those of the QPM.

An alternative Monte Carlo program that incorporates the parton shower approach is HERWIG [16]. In this model the parton shower takes place inside a cone of angular size set by the incoming and outgoing struck parton. In DIS, this correlates the initial and final parton showers. The characteristic scale of the parton shower is given by $2E^2(1-\cos\psi)$ where E is the energy of the parton and ψ is the angle with respect to its colour connected partner.

The parton showers in both LEPTO and HERWIG are simulated in the LLA. The technique used to simulate final state partonic radiation [16, 17] is the same as that used to describe e^+e^- annihilation, where it is well tested experimentally [2]. The simulation of initial state radiation [16, 18], however, is not well tested and is also dependent on the parton densities in the proton.

LEPTO also allows the possibility of adding parton showers to the first order matrix element (ME+PS) [19]. This option gives the exact first order hard emissions in the BGF and QCDC processes and, in addition, limits the choice of virtuality scale for the parton showers. If the matrix element gives no radiation, then the choice of scale for the softer emissions is determined by the m_{ij} cutoff used in the matrix element calculation. An event originating from a first order process has a maximum virtuality for the final state radiation set by the invariant mass of the resulting partons.

A different approach to the problem of describing the partonic final state is provided by the colour dipole model (CDM). In this model, the struck quark and the proton remnant are considered to form a colour dipole. When this dipole radiates a gluon, it splits into two radiating dipoles: one between the struck quark and the gluon and the other between the gluon and the remnant. Repeated gluonic emissions lead to a chain of such dipoles. Unlike the e^+e^- case, in DIS one end of the dipole system is not point-like since the proton remnant is an extended object. As a result, the maximum p_T^2 in the hadronic centre of mass system for an emitted gluon varies as $W^{\frac{4}{3}}$ [20]. For DIS, the simulation of the QCDC process is only approximate because of the extended proton remnant. The dipole model is coded in the program ARIADNE [21], which in turn is interfaced to that part of LEPTO which generates the hard scattering.

Since the boson-gluon fusion process is not accounted for in the CDM, the provision has been made in ARIADNE to include this process as given by the first order matrix element. This will be referred to as CDM+BGF. In this option, the produced quark and anti-quark each form

independent dipoles with the remnant system. The first gluon emission in e^+e^- annihilation is exactly simulated by the dipole radiation.

First order electroweak radiative cross sections are calculated in the program HERACLES [22] which is interfaced [23] to LEPTO as well as to ARIADNE. This program chain allows fragmentation and QCD cascades to be studied in radiative events. The ME, ME+PS, and CDM+BGF models were investigated without electroweak radiative corrections. All these programs work within the framework of the Lund string model [24] where the hadrons are formed along colour flux tubes stretched between the outgoing partons. This hadronization method is implemented in the JETSET program [25].

The hadronization in HERWIG is based on a scheme where the partons formed late in the shower are combined into low mass, colourless clusters which then decay isotropically. Any heavier clusters are first allowed to decay into two lighter clusters in a manner similar to that used in the Lund string. HERWIG was investigated without electroweak radiative corrections.

There is no clear theoretical prescription for dealing with the proton remnant and this leads to major differences between the predictions of the different models. In the LEPTO versions of the Lund string model, simple quark counting is used [26] for the remnant treatment. For scattering off a valence quark the remnant is taken to be the resulting diquark. For a sea quark scatter the remnant is split into either a baryon and a quark or a meson and a diquark. For the BGF process the three valence quarks in the remnant are divided into a quark and a diquark. In HERWIG two approaches are available. The default choice uses a soft underlying event (SUE) based on a phenomenological description of minimum bias events from the UA5 experiment [27]. This method splits the remnant into many 'soft' clusters. The other technique allows the remnant to only split into two clusters.

Event samples generated by the above Monte Carlo methods were processed with the ZEUS detector simulation program, a trigger simulation and the offline reconstruction procedure. Electronic and uranium noise in the calorimeter was simulated. The detector simulation is based on the general purpose program GEANT3.13 [28]. The description of the responses of the various detector components was tuned to reproduce test beam data. The Monte Carlo event samples were subjected to the same selection procedure applied to the data.

6 Results

A series of calorimeter cell energy distributions is used to compare the data with the predictions of the Monte Carlo models described above. Each calorimeter cell defines a vector, $\vec{E}$, with direction given by the geometrical centre of the cell and magnitude by the energy deposit. In order to study the x dependence of QCD radiation, the distributions are plotted in three different x bins indicated in figure 1a: $x < 10^{-3}$, $10^{-3} < x < 10^{-2}$, and $x > 10^{-2}$. The highest bin is close to the x region covered by existing data, whereas the lowest x region only becomes accessible at HERA energies. In all of the comparisons, cells with $\vartheta < 10^\circ$ are removed to reduce the influence of the proton remnant. The error bars on the data are statistical and are within the symbols if they are not shown. Systematic checks on the Monte Carlo event samples are discussed in the following section. All the Monte Carlo samples shown were generated with the MRSD0 parton density parametrization [29].

The energy flow distributions as a function of the polar angle, ϑ, are shown in figure 2 for the three x regions and for different W^2 selections. In the lowest x range, figure 2a, the jet energy peak at large angles is clearly visible superimposed on a falling distribution at small angles. With HERA kinematics, at fixed x the current jet swings from the forward to the backward region as the W^2 values increase. This is illustrated in figures 2(b-d), showing results in the intermediate x range. At high x, shown in figure 2e, the data exhibits a smooth fall with ϑ since for most of the events the hadronic system has a high energy and populates the forward region. In all cases, however, the energy is distributed over the full range of polar angles.

The transverse energy flow of the hadronic system is shown in figure 3. To illustrate better the model comparisons, the same data are shown separately in two sets of three x−range plots. These distributions show transverse energy weighted azimuthal angles, ϕ, where $\phi = 0^\circ$ is defined by the direction of the scattered electron. The transverse energy, E_T, of each cell is given by $E \sin\vartheta$. In all cases the data peak at $\phi = 180^\circ$ with the hadrons balancing the E_T of the electron. This is particularly clear in the two higher x bins. In the lowest x region, the data show a broader E_T distribution. In addition, the total E_T, which is the area of each distribution, increases as x decreases, i.e. as W increases.

The histograms in figures 3(a-c) show the predictions of several different models. The first order matrix element calculation (dashed-dotted histogram) predicts a distribution that is more peaked in ϕ than is observed, particularly at the lower x values. This poor agreement between the data and the predictions of the first order matrix elements highlights the need to take into account higher orders in α_s. The PS(W^2) model (dashed histogram) reproduces the general shape of the data but much overestimates the E_T. On the other hand, the PS(Q^2) approach (dotted histogram) predicts even less E_T than the matrix elements, particularly at the lower x values. The ME+PS model (full histogram) gives a good description of the E_T distributions of the data. Since the PS(Q^2) choice yields little gluon radiation, the comparison of the data with the predictions of this model suggests that the observed broadening of the event structure in the transverse plane is due not to kinematics but primarily to QCD radiation.

The different behaviour predicted by the W^2 and Q^2 choices of the virtuality scale, shown in figure 3a, can be understood from equation (5): at low x, the values of W^2 are much larger than those of Q^2, thus allowing more gluon radiation. For the highest x region, however, the predictions of all parton shower models are similar since the Q^2 and W^2 values are more similar. In this region all models give a reasonable representation of the data.

The PS($Q^2(1-x)$) choice (dotted histogram) is shown in figures 3(d-f). It gives a good description of the data in the two highest x bins, but predicts too little E_T at low x. The comparisons with the CDM (dashed histogram), and CDM+BGF models (full histogram), along with the HERWIG model without the SUE (dashed-dotted histogram), are also shown in these figures. It is clear that these models are in reasonable accord with the E_T distributions of the data. The HERWIG prediction including the SUE (not shown) is similar.

To study the transverse energy arising from gluon radiation, the energy component perpendicular to the scattering plane, $(E_t)_{out}$ was measured. The scattering plane contains the Z-axis and an axis that was determined by maximizing the E_t in that plane, $(E_t)_{in}$, of all the cells (including those associated with the found electron). In the QPM, this is the plane that contains the beam axis, the scattered electron and the struck quark.

In figure 4 the mean $(E_t)_{out}$ of the hadronic system is shown as a function of W^2 for the different x bins. The data show an increase of $(E_t)_{out}$ as W^2 increases. This might be expected

since an increase in W^2 at fixed x means that the energy is not taken by the remnant and is therefore available for QCD radiation. These comparisons with the Monte Carlo models show the same general trends seen in the previous comparisons. Again, the PS(Q^2), PS(W^2), and ME predictions are in poor agreement with the data, whereas the CDM, ME+PS, and HERWIG predictions are in general agreement with the data, although some deviations are evident at high x and high Q^2.

A more sensitive display of the energy flow for the low x region is shown as a function of pseudorapidity in figure 5. The pseudorapidity, η, is given by $\eta = -ln\left(\tan\left(\frac{\vartheta}{2}\right)\right)$. This plot shows the energy weighted pseudorapidity difference between the calorimeter cell and that of the hadron angle γ_h, the direction of the scattered quark in the QPM, $\Delta\eta = \eta - \eta_{\gamma_h}$. Note that for a γ_h at the RCAL/BCAL boundary, the 10° beampipe cut corresponds to a $\Delta\eta$ of ≈ 3.1 so that the shape of the peak at large $\Delta\eta$ is influenced by this cut. The fall off at negative values of $\Delta\eta$ is not affected by the rear beam pipe, which is near $\Delta\eta = -1.5$. It is striking that almost all of the energy appears at positive values, between the direction of γ_h and that of the proton remnant. Such a behaviour is expected from the gluon radiation that should be concentrated in this angular range. For this low x range, there is a continuous distribution of energy flow from that associated with the struck quark to that coming from the proton remnant even though γ_h points in the direction of the RCAL, i.e. opposite to the direction of the proton remnant, as can be seen in figure 1a. In addition, a shift in the peak from the expectation of the QPM model ($\Delta\eta = 0$) is clearly seen.

The predictions of PS(W^2) (dashed histogram), PS(Q^2) (dotted histogram), and ME (dashed-dotted), shown in figure 5a, do not reproduce the data. The peaks in the PS(Q^2) and ME distributions are centered at γ_h ($\Delta\eta \approx 0$), thus indicating that the shift in the data is in fact due to QCD radiation. The ME+PS prediction (full histogram) is in better agreement with the data near $\Delta\eta = 0$ although the peak is somewhat broader than that observed. This prediction falls below the data in the large $\Delta\eta$ region. However, in this region the model prediction is sensitive to the y_{cut} parameter. In this plot we have used a value of 0.01; the prediction with the default value of 0.015 underestimates the data even more.

The CDM models are compared to the data in figure 5b. Both the CDM (dashed histogram) and the CDM+BGF (full histogram) give a better representation of the data than the other models, particularly at large $\Delta\eta$. However, these models somewhat overestimate the energy in the region between the quark and the proton remnant. The PS($Q^2(1-x)$) model is shown as the dotted histogram in figure 5b. It reproduces the peak at $\Delta\eta = 0$ better than either the PS(W^2) or PS(Q^2) models, but predicts too little energy for $\Delta\eta > 1$. It must be stressed that these differences in the Lund models in the larger $\Delta\eta$ region are due solely to differences in the treatment of QCD radiation because all models use the same hadronization of the proton remnant.

Figure 5c shows the predictions of the HERWIG model both with (dashed histogram) and without (solid histogram) the SUE. The latter is in equally good agreement with the measurements as the CDM+BGF model whereas the prediction with the inclusion of an underlying event overestimates the energy flow in the large $\Delta\eta$ region.

7 Systematic Checks

To investigate whether these conclusions are sensitive to the details of the models, various checks were made. The FCAL energy requirement of 1 GeV, applied after the other event selection cuts, rejected about 1% of the events in all of the Monte Carlo samples, with one exception. It removed about 4% of the events from the data sample. The exception was HERWIG without the SUE, for which the fraction of events rejected was considerably higher. A study of these events showed that the partonic final state usually contained only a struck quark and a proton remnant with the latter remaining in the forward beam pipe.

To study the effects of the electroweak radiative corrections, the predictions of ARIADNE calculated both with and without the interface to HERACLES were compared. The shifts observed in the distributions were negligible compared to the large differences in the predictions of the various models.

The dependence of the predictions of the parton shower and matrix element models on the parton density parametrization was studied by using two sets by Morfin and Tung (MTB1 and MTB2) [30] and two sets by Martin, Roberts and Stirling (MRSD0 and MRSD−) [29]. For all plots, the differences were smaller than the statistical errors in the data.

The sensitivity of the PS and ME predictions to model parameters was also studied to determine if the observed differences between the data and model predictions could be reduced by parameter tuning. The *minimum* virtuality of 1 GeV in both the initial and final state parton showers was increased and decreased by a factor of three. This is the virtuality at which partons are assumed to be on mass-shell. The Λ parameter of the strong coupling constant used in both the initial and final state showers was also varied by a factor of three. In addition, the Gaussian width of the primordial transverse momentum distribution of the partons within the proton was varied. The effect of the fragmentation was checked by changing the parameters that govern the energy-momentum fraction and the p_T distributions of the primary produced hadrons in the Lund string model. The transverse energy flow plots were the most sensitive to these changes. Nevertheless, the effects were, again, always smaller than the statistical errors. The ME model is sensitive to the y_{cut} parameter in the forward region. An increase from 0.0025 to 0.015 decreases the prediction for the energy deposited in the $10° - 20°$ region by appoximately 10%. However, the transverse energy flow has little sensitivity to this parameter. We note that these variations are larger than those made in tuning the values [14] to match lower energy data.

The electron identification algorithms can introduce a systematic error for various reasons. One is that the algorithms have differing purities for accepting DIS events compared to possible photoproduction background which mainly occurs in the low Q^2, low x regions. Another is related to the assignment of calorimeter cells to the electron. The difference between different algorithms exhibited small effects on the general overall shape of the distributions and do not alter any of the conclusions drawn. By increasing the energy cut on the found electron from 5 GeV to 10 GeV, possible photoproduction background is reduced. This change does not alter the overall trends of the distributions so that the conclusions are unchanged. The estimated photoproduction backgound is 10% in the lowest x region and 3% overall.

The effect of varying the hadronic energy scale by ±5% was smaller than the statistical errors. The detector simulation shows that energy corrections due to dead material and the smearing coming from resolution and acceptance effects were about 20% for most of the distributions.

8 Summary

We have presented measurements of hadronic energy distributions in DIS at HERA. For decreasing x an increase in E_T of the hadronic system, with respect to the proton direction, is observed as well as a general broadening of the energy flow in the transverse plane. In the low x region, the peak in the hadronic energy flow in the direction of the current jet is shifted from the position expected by the QPM towards the proton remnant with most of the energy appearing between the position of the expected jet peak and that of the proton remnant.

The comparisons with the data show that the Lund model, in which the first order matrix elements are combined with parton showers, gives a reasonable description of the energy flows. The predictions of the colour dipole and the HERWIG parton shower models also agree with the overall trends of the data.

By contrast, the predictions of a model based on the first order matrix elements alone are in disagreement with observation. Furthermore, in the Lund parton shower model alone, neither the choice of W^2 nor Q^2 to set the virtuality scale for the parton showers can describe the final hadronic states. The scale $Q^2(1-x)max(1,\ln\frac{1}{x})$, motivated by the behaviour of the matrix elements, also fails. The differences cannot be accounted for by changes in the fragmentation parameters, model parameters, or present parton density parametrizations.

Acknowledgements

The strong support and encouragement by the DESY Directorate have been invaluable.

The experiment was made possible by the inventiveness and the diligent efforts of the HERA machine group who succeeded in making HERA run.

The design, construction and installation of the ZEUS detector have been made possible by the ingenuity and dedicated effort of many people from inside DESY and from the home institutes who are not listed as authors. Their contributions are acknowledged with great appreciation.

We would like to thank G. Ingelman, I. Knowles, L. Lönnblad, and B. Webber for fruitful dialogue on various aspects of the Monte Carlo models.

References

[1] H1 collab., T. Ahmed et al., Phys. Lett. B298(1993) 469.

[2] OPAL collab., M.Z. Akrawy et al., Z. Phys. C47(1990) 505.
L3 collab., B. Adeva et al., ibid. C55(1992) 39.
ALEPH collab., D. Buskulic et al., ibid. 209.
W. deBoer and H. Fürstenau, Proc. of MC91 Workshop, NIKHEF(1991) 616.

[3] EMC collab., J.J. Aubert et al., Phys. Lett. B95(1980) 306, ibid. B100(1981) 433, Phys.Lett. B119(1982) 233.
E665 collab., M.R. Adams et al., Phys. Rev. Lett 69(1992) 1026.

[4] EMC collab., M. Arneodo et al., Z. Phys. C36(1987) 527.

[5] ZEUS collab., M. Derrick et al., DESY 93-030, Phys.Lett. B to be published.

[6] ZEUS collab., M. Derrick et al., Phys. Lett. B303(1993) 183.

[7] C.B. Brooks et al., Nucl. Inst. Meth. A283 (1989) 477.
N. Harnew et al., ibid. A279 (1989) 290.

[8] M. Derrick et al., Nucl. Inst. Meth. A309 (1991) 77.
A. Andresen et al, ibid. 101.

[9] A. Bernstein et al. To be submitted to Nucl. Inst. Meth. U. Mallik, Proc of International Conference on High Energy Physics, Fermilab(1990).

[10] D. Graudenz and N. Magnussen, Proc. of Physics at HERA vol. 1, DESY(1992).

[11] M. Bengtsson, G. Ingelman and T. Sjöstrand, Nucl. Phys. B301(1988) 554.
M. Bengtsson and T. Sjöstrand, Z. Phys. C37(1988) 465.

[12] G. Marchesini and B.R. Webber, Nucl. Phys. B310(1988) 461.

[13] G. Gustafson, Phys. Lett. B175(1986) 453.
G. Gustafson and U. Pettersson, Nucl. Phys. B306(1988) 746.

[14] N. Magnussen et al., Proc. of the Workshop on Physics at HERA, vol. 3, DESY (1992).

[15] G. Ingelman, Proc. of Workshop on Physics at HERA vol. 3, DESY, (1992).

[16] G. Marchesini et al., Comp. Phys. Comm. 67 (1992) 465.

[17] M. Bengtsson and T. Sjöstrand, Phys. Lett. B185(1987) 435.

[18] T. Sjöstrand, Phys. Lett. B157(1985) 321.

[19] N. Brook, G. Ingelman and L. Lönnblad, Proc. of Workshop on Physics at HERA vol 1., DESY, (1992).

[20] B. Andersson et al., Z. Phys. C43(1989) 625.

[21] L. Lönnblad, Lund preprint, LU TP-89-10.
L. Lönnblad, Comp. Phys. Comm. 71(1992) 15.

[22] A. Kwiatkowski, H. Spiesberger and H.-J. Möhring, Proc. of Workshop on Physics at HERA vol. 3, DESY, (1992).

[23] G. Schuler and H. Spiesberger, Proc. of Workshop on Physics at HERA vol. 3, DESY, (1992).

[24] B. Andersson et al., Phys. Rep. 97(1983) 31.

[25] T. Sjöstrand, Comp. Phys. Comm. 39 (1986) 347.
T. Sjöstrand and M. Bengtsson, ibid. 43 (1987) 367.

[26] B. Andersen et al., Z. Phys. C13(1982) 361.

[27] UA5 collab., G.J. Alner et al., Nucl. Phys. B291 (1987) 445.

[28] R. Brun et al., CERN DD/EE/84-1 (1987).

[29] A.D. Martin, R.G. Roberts and W.J. Stirling, Durham/RAL preprint, DTP-92-16 and RAL-92-021, to be published in Phys. Rev. D.

[30] J. Morfin and W.K. Tung, Z. Phys. C52(1991) 13.

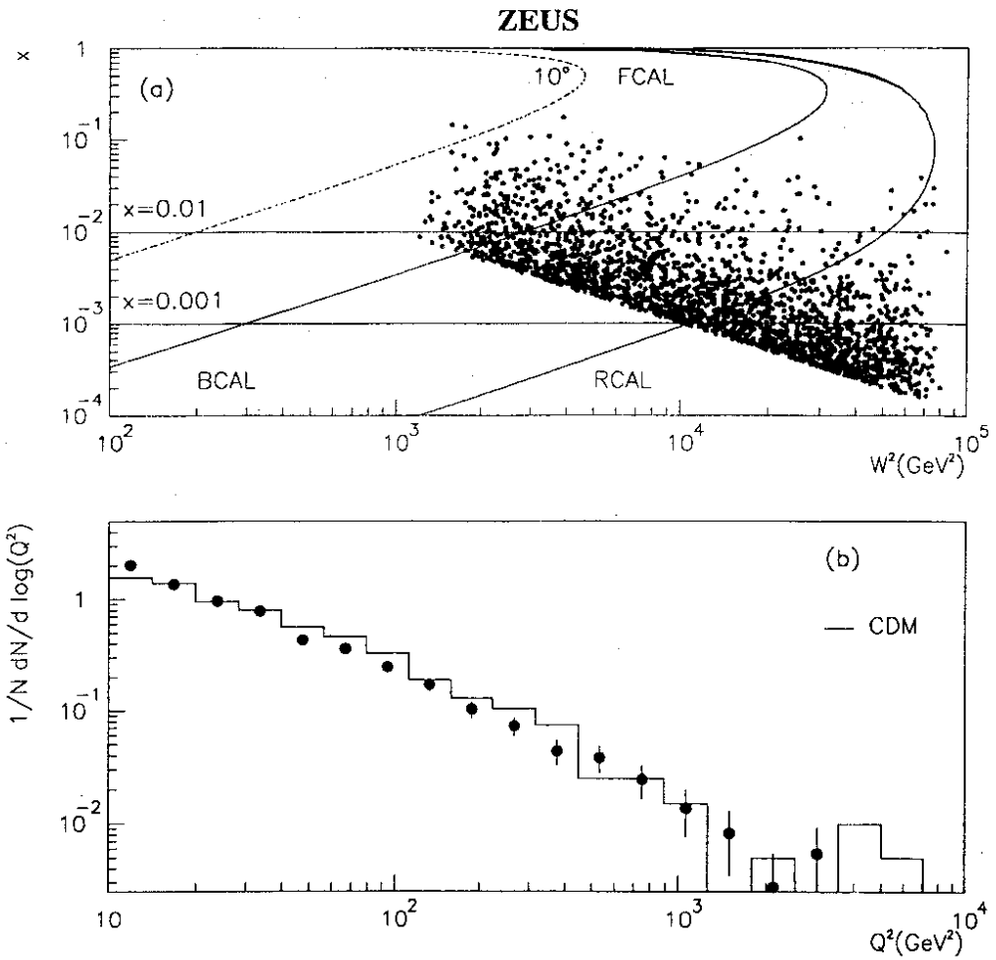

Figure 1: (a) The $W^2 - x$ distribution of the ZEUS data marked with the x bins used in the analysis. The contours of the angles, γ_h, corresponding to the boundaries of the calorimeter components are shown as the full lines. The dashed curve, at low W^2 and high x, corresponds to a 10° contour. (b) The Q^2 distribution. All the variables have been calculated from the double angle method. The histogram shows the HERACLES+ARIADNE (CDM) Monte Carlo discussed in the text.

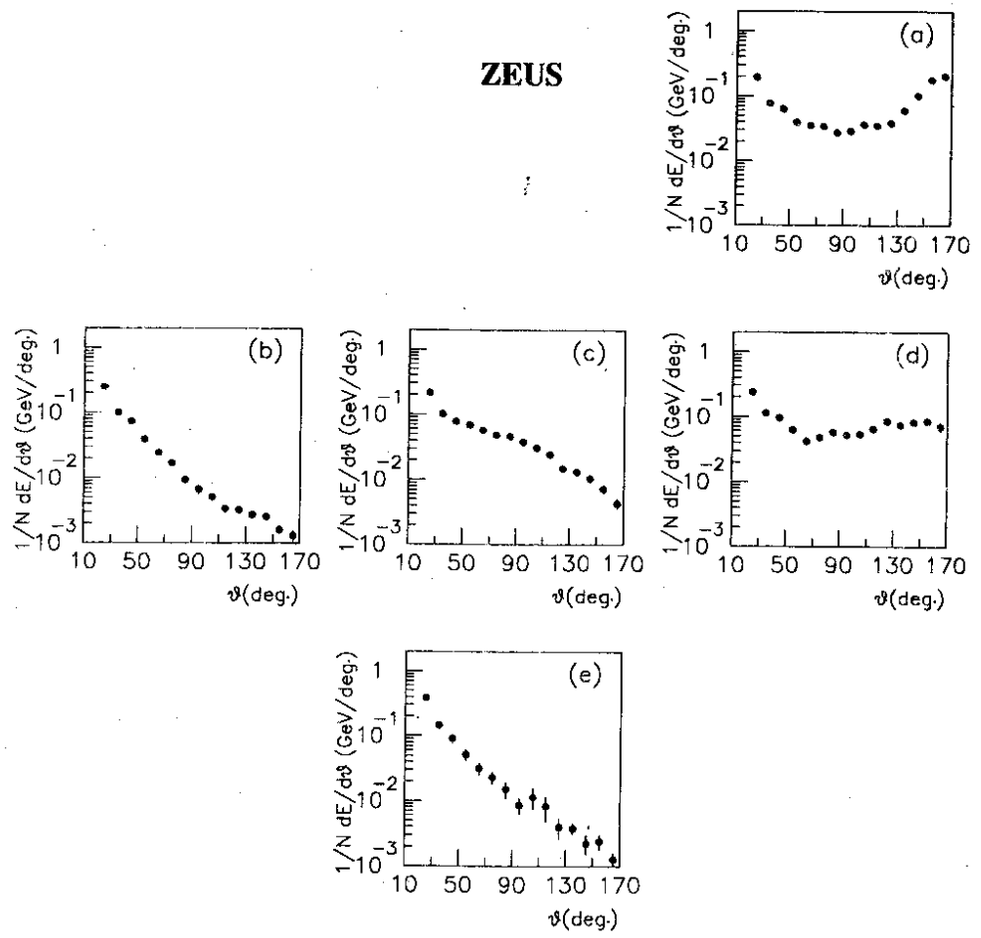

Figure 2: The energy weighted ϑ distributions in the ranges of x and W^2 used in this analysis. In (a) $x < 0.001$ and $15000 < W^2 < 60000\ GeV^2$. In (b)-(d) $0.001 < x < 0.01$ with $1000 < W^2 < 7000\ GeV^2$, $7000 < W^2 < 15000\ GeV^2$ and $15000 < W^2 < 60000\ GeV^2$ respectively. In (e) $x > 0.01$ and $1000 < W^2 < 60000\ GeV^2$.

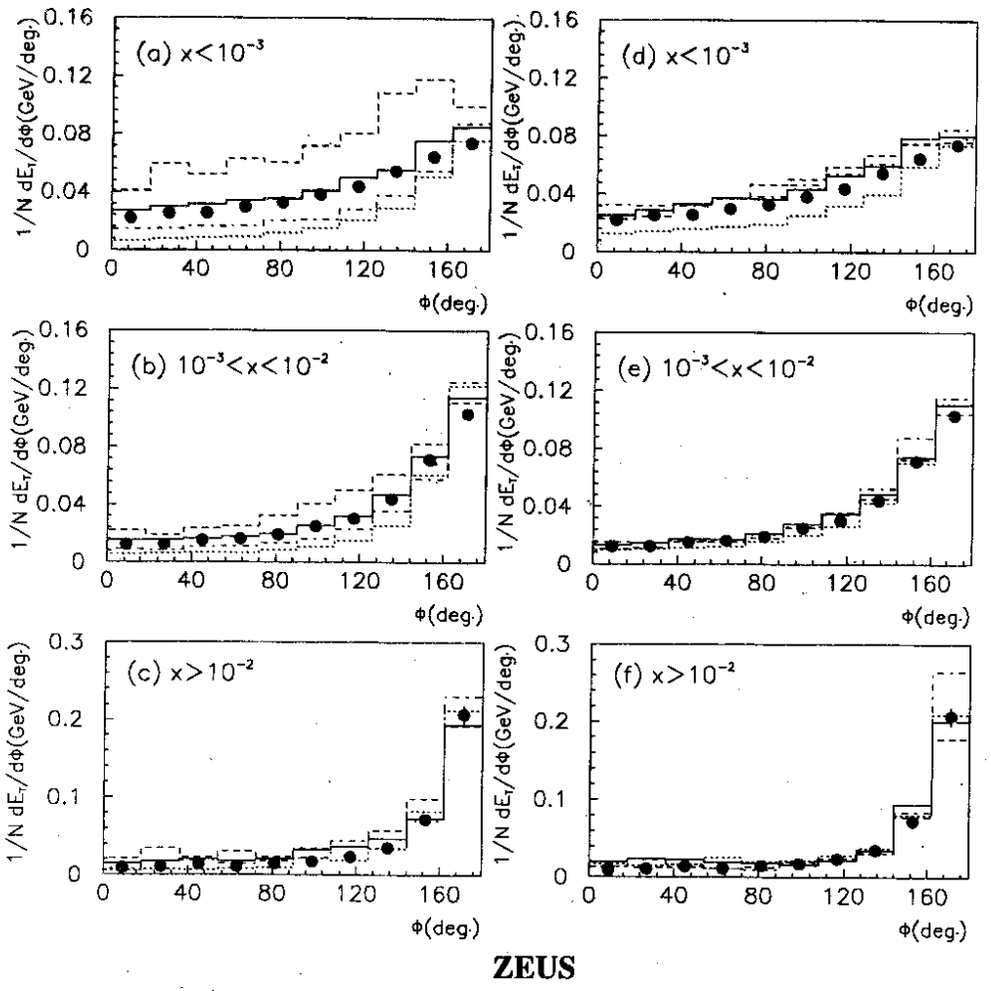

Figure 3: The transverse energy weighted azimuthal angular distributions in the three ranges of x: $x < 10^{-3}$, $10^{-3} < x < 10^{-2}$ and $x > 10^{-2}$. The scattered electron is defined as $\phi = 0$. The ZEUS data points are shown as the dots. In (a), (b) and (c) the full histogram is ME+PS, the dashed histogram PS(W^2), the dotted histogram PS(Q^2), and the dash-dotted histogram ME. In (d), (e) and (f) the full histogram is CDM+BGF, the dashed histogram CDM, the dotted histogram PS($Q^2(1-x)$) and the dash-dotted histogram HERWIG.

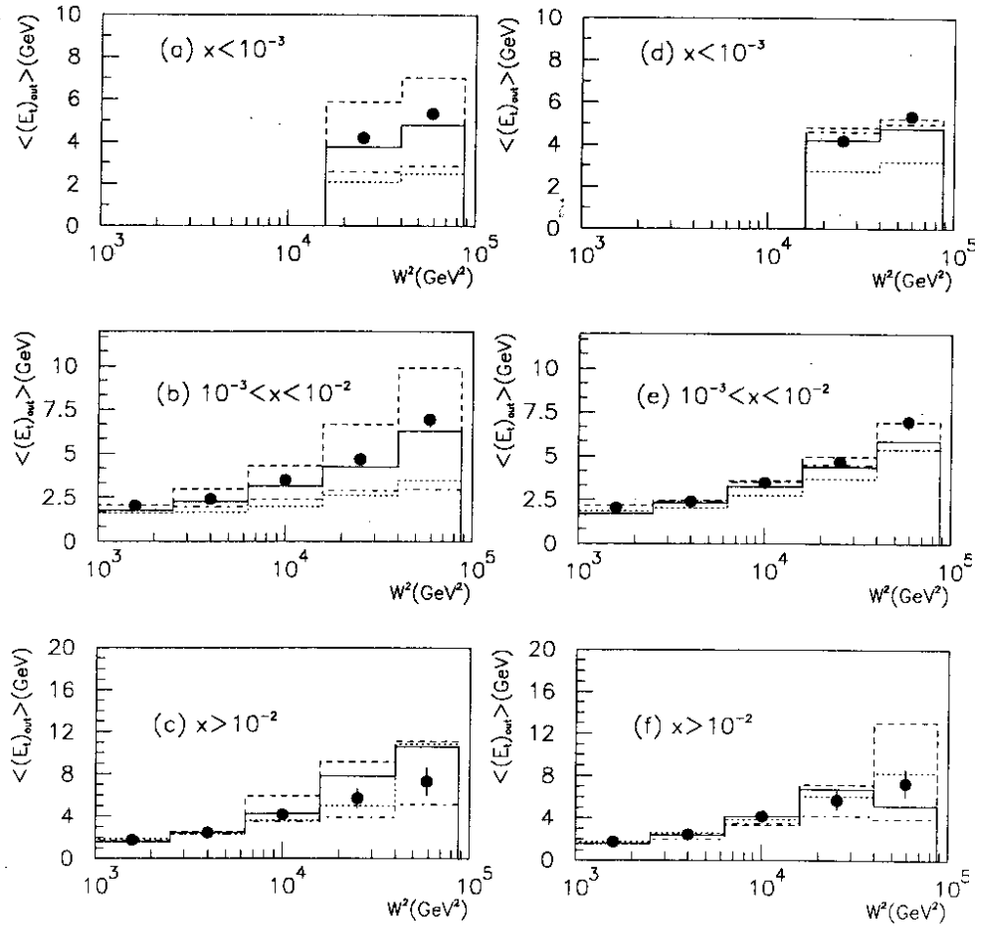

Figure 4: The mean $(E_t)_{out}$ as a function of W^2 in the three ranges of x: $x < 10^{-3}$, $10^{-3} < x < 10^{-2}$ and $x > 10^{-2}$. The ZEUS data points are shown as the dots. In (a), (b) and (c) the full histogram is ME+PS, the dashed histogram PS(W^2), the dotted histogram PS(Q^2), and the dash-dotted histogram ME. In (d), (e) and (f) the full histogram is CDM+BGF, the dashed histogram CDM, the dotted histogram PS($Q^2(1-x)$) and the dash-dotted histogram HERWIG.

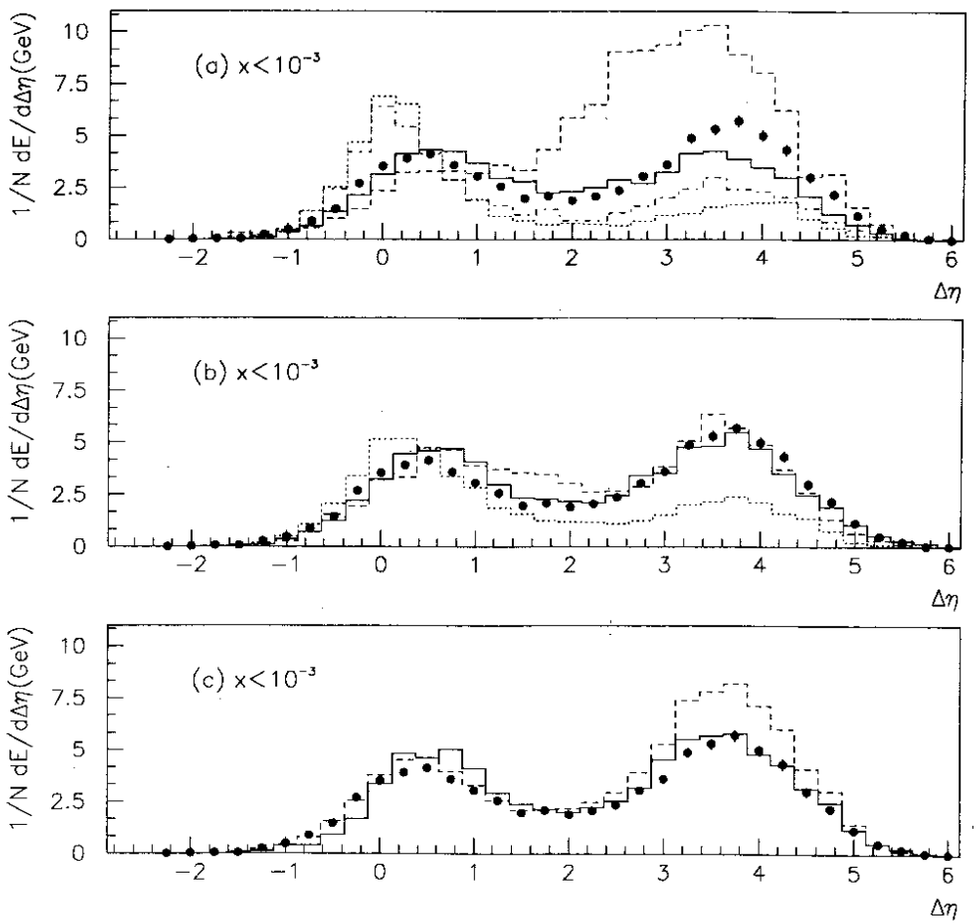

Figure 5: The energy weighted pseudorapidity difference, $\Delta\eta$, of the hadronic system calorimeter cells with respect to the struck quark from the quark-parton model. The ZEUS data points are shown as the dots. In (a) the full histogram is ME+PS, the dashed histogram PS(W^2), the dotted histogram PS(Q^2), and the dash-dotted histogram ME. In (b) the full histogram is CDM+BGF, the dashed histogram CDM and the dotted histogram PS($Q^2(1-x)$). In (c) the full histogram is HERWIG without the SUE and the dashed histogram HERWIG including the SUE.